J Seismol (2012) 16:777–786
DOI 10.1007/s10950-012-9283-x

ORIGINAL ARTICLE

High-frequency noise caused by wind in large ring laser gyroscope data

A. Gebauer · K. U. Schreiber · T. Klügel · N. Schön · U. Ulbrich

Received: 29 July 2011 / Accepted: 6 February 2012 / Published online: 26 February 2012

Abstract The large ring laser gyroscope at the Geodetic Observatory Wettzell provides unique data of the rotational component of seismic waves. Wind has been identified as a major source of noise at short periods below 5 min. Strong winds increase the level of detected background noise either through surface friction or through wind load on hill slopes. Since our G ring laser demonstrated a routinely achieved sensitivity for rotations of 10 picorad/s when averaged over 30 s, very small effects become detectable. Using a local finite element model and applying a digital terrain model with 25 m spatial resolution, the effect of local wind forces on tilt and horizontal rotations at the ring laser site was calculated. The transfer of forces by wind ram pressure or surface friction is strongly controlled by the resolution of the terrain model or the land use, respectively. The maximum deformation caused by real wind fields reaches a few tenths of nanorads for both tilt and horizontal rotation. While the tilts are too small to affect the ring laser measurements by a change in its inclination, the horizontal rotations can be detected by the ring laser if the signal builds up within a few seconds or tens of seconds. The comparison of the modelled rotation rate time series with measured ring laser data shows a reasonable agreement in amplitude and waveform, however the correction of the ring laser time series is limited by the crude sampling of the wind measurements.

Keywords Ring laser · Seismology · Finite element models · Crustal deformation

This study is also found in the Proceedings to the 2nd International Working Group on Rotational Seismology (IWGoRS) workshop.

A. Gebauer (✉)
Geodetic Observatory Wettzell,
Technical University Munich,
Sackenrieder Straße 25,
93444 Bad Kötzting, Germany
e-mail: gebauer@fs.wettzell.de

K. U. Schreiber · T. Klügel
Geodetic Observatory Wettzell,
Federal Agency for Cartography and Geodesy,
Sackenrieder Straße 25,
93444 Bad Kötzting, Germany

K. U. Schreiber
e-mail: schreiber@fs.wettzell.de

T. Klügel
e-mail: kluegel@fs.wettzell.de

N. Schön · U. Ulbrich
Institute of Meteorology, Free University Berlin,
Carl-Heinrich-Becker-Weg 6-10,
12165 Berlin, Germany

N. Schön
e-mail: nana@gfz-potsdam.de

U. Ulbrich
e-mail: ulbrich@met.fu-berlin.de

1 Introduction

Ring lasers are gyroscopes measuring absolutely the magnitude of each rotation component acting along its sensitive axis. The large ring laser “G”, located in an underground laboratory at the Geodetic Observatory Wettzell (Bavaria), has been constructed to monitor variations in Earth rotation. It measures rotational signals over a wide spectral range. Currently the measurement signals cover periods from 435 days (Chandler wobble) on one end of the spectrum to less than 5 ms (20 Hz) for rotational signals from local seismic events. It is a unique instrument to study rotational components of seismic surface waves (Suryanto et al. 2006) or toroidal modes of the Earth's free oscillations (Igel et al. 2011). The global signals coming from tidal tilt and polar motion are extensively investigated by Schreiber et al. (2003, 2004, 2011), Klügel et al. (2008) and Velikoseltsev et al. (2008).

The basic concept of ring lasers for geophysical applications is described in Stedman (1997). Two counter propagating laser beams in a square laser cavity experience a frequency shift due to rotation. The resulting beat frequency, or Sagnac frequency, is

$$\delta f_{\mathrm{Sagnac}} = \frac{4A}{\lambda P}\vec{n}\vec{\Omega}, \tag{1}$$

where A is the area, P the perimeter and λ the wavelength of the helium/neon laser transition. $\vec{\Omega}$ is the imposed rate of rotation (in our case the Earth rotation rate), and $\vec{n}$ represents the normal vector on the plane of the laser cavity. The expression $4A/\lambda P$ is also referred to as the scale factor of the ring laser structure. The scale factor determines the ultimate resolution of the ring laser, but more than that, it also defines the stability of the measurement device, because scale factor variations directly map into the measured signal. The "G" ring laser having a size of 4×4 m currently has a relative scale factor stability of $\approx 5\times10^{-9}$, with an applied averaging time of 1 h, corresponding to a beat frequency of approximately 4 μHz or a rotation rate of 7×10^{-13} rad/s taking the spinning rate of the Earth as reference. A detailed description of the "G" ring laser is given in Schreiber et al. (2009).

Variations in orientation of both the sensor normal axis and the rotation axis of the Earth are mapped into the measurement signal via the inner product of Eq. 1. Orientation changes of about 10 nrad are still detectable in our apparatus. Hence the monitoring of the local tilt of the ring laser is of special interest. As significant tilts of different origin are present even at greater depth (e.g. Weise 1992; Klügel 2002), highresolution platform tiltmeters are permanently monitoring the orientation of the ring laser in order to reduce the local tilt effect. The signal content of tiltmeters can be classified according to Kümpel (1982). Non-tidal transient tilts are often identified to be of hydrological origin (e.g. Weise 1992), while barometric pressure load contributes to tilt up to 20 nrad (Gebauer et al. 2010; Kroner et al. 2005; Steffen 2006). Striking transient signals in tiltmeters frequently occur during passing thunderstorms, which may have different causes like air mass attraction, barometric loading or wind.

While barometric effects are successfully investigated, the modelling of wind-induced deformations is much more difficult due to the uncertainty in the shear transfer mechanism and parameters. Pure meteorological approaches aiming on the estimation of coefficients for pressure drag and surface roughness at large scales were carried out by Emeis (1987) and Emeis and Zilitinkevich (1991). Large-scale wind and barometric effects on the "G" ring laser were investigated by Velikoseltsev et al. (2009) using a finite element (FE) model for Central Europe, however no significant correlation between modelled wind effects and ring laser signals were found.

In this approach small-scale effects acting at higher frequencies are investigated. The considered time scale ranges from seconds up to several minutes. The estimation of the Sagnac frequency yields one data point each 30 s. The standard deviation of the 30 s data over 30 min (Fig. 1) typically varies between 10 and 20 μHz during quiet periods, while noisy epochs are indicated by an increase of the standard deviation up to 80 μHz. By comparison with local wind speed observations, it is obvious that wind is responsible for most of the high-frequency noise, which affects the analysis of ring laser data with respect to seismological signals. Another source of noise are oceanic microseisms reaching amplitudes up to 100 picorad/s or 500 μHz in the period range 5–10 s (e.g. Hadziioannou et al. 2012). However, due to the integration of the Sagnac frequency over 30 s, the microseisms are averaged out and only weakly present in our data set. Human-made noise is mostly limited to discrete events like nearby crossing trucks or construction activities

The effect of local wind becomes even more clear in the spectral domain. The Fourier spectrum of a 29-h data set of a windy day and a quiet day is shown in Fig. 2. The overall energy on a windy day is about four times larger than on a quiet day, especially at higher frequencies. If the wind effect on the ring laser can be understood and properly modelled, another undesired signal could be removed thus improving the signal to noise ratio. In this paper the effect of surface deformations caused by wind loads on the "G"

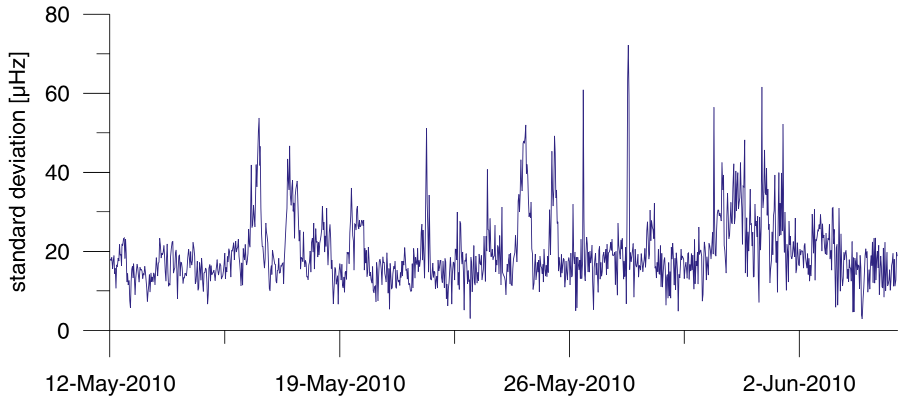

Fig. 1 Standard deviation of the Sagnac frequency measurement from averaged 30-s values over 60 samples

ring laser is quantified using a highly resolved local finite element model.

2 Definition of the FE model

A FE model of the Wettzell region (Fig. 3) was created using the software packages '*Abaqus*' (Abaqus Inc. 2007) and '*HyperMesh*' (Altair Engineering Inc. 2008). A detailed description of the procedure is found in Gebauer (2009). The model represents a crustal block of 20×20×4.5 km in east–west, north–south and vertical direction, respectively. The topography was taken from a digital terrain model (DTM) having a horizontal resolution of 25 m ("DGM25", BKG; DTM-25 2010). The FE model consists of about two million tetrahedral elements. The element size at the top surface where the load is applied is about 22 m in order to have a good approximation of the orography and to have at least one node in each cell of the DTM. The element size decreases towards the middle of the model to less than 5 m at the location of the ring laser "G" to avoid discretization errors. Towards the model bottom the element size increases up to 200 m. The boundary conditions are chosen in a way that the nodes at the model bottom must not move in vertical direction, and the nodes at the vertical boundaries must not move in horizontal direction, i.e. perpendicular to the model sides.

The FE model is parameterized homogenously using elastic parameters which are derived from laboratory and in situ measurements. For a fresh sample of crystalline bedrock from a depth of 25 m, a Young's modulus of 58 GPa and a Poisson ratio of 0.26 was determined in a triaxial compression test. However, in

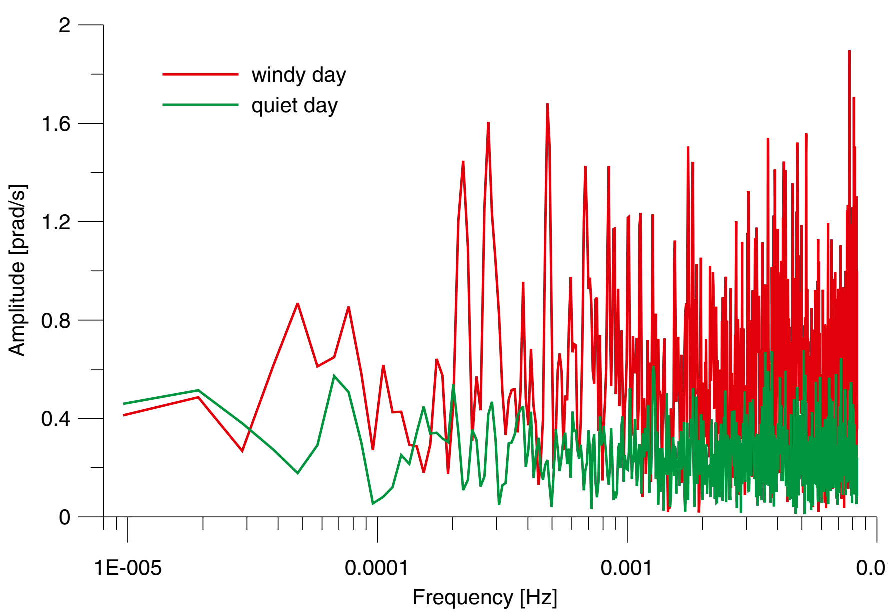

Fig. 2 Fourier spectrum of 30 s sampled, high-pass filtered Sagnac frequency data converted into rotation rate, 29 h of a quiet and a windy day

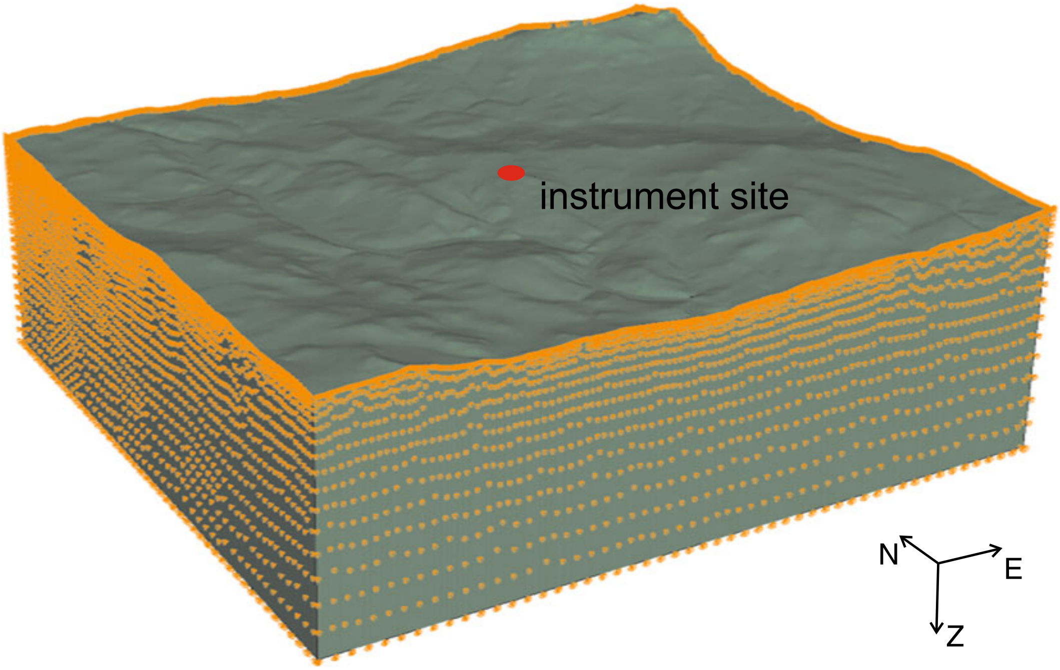

Fig. 3 Assembly of the FE model used to estimate the wind-forced rotations. The ring laser site at the Geodetic Observatory Wettzell is at the surface in the middle. The *orange triangles* at the vertical model boundaries mark the nodes of the mesh

situ measurements (borehole extension tests) in depths between 10 and 35 m yield much smaller values of the Young's modulus ranging between 1 and 12 GPa (Klügel 2001), which is the consequence of joints and fractures in the rock.

Consequently a Young's modulus of 7 GPa and a Poisson ratio of 0.25 was chosen for the model taking into account that the main energy transfer caused by the wind happens in a few metres below the surface. As a linear elastic rheology is assumed, all results can be scaled linearly according to the load which is actually applied.

3 Loading of the FE model

The wind load is applied to the model as a force directly at the nodes. Depending on the location, the magnitude and the direction of the force to be applied at the model surface were calculated. The force $F_{w(i,j)}$ (Eq. 2) is the sum of the wind pressure on the topography (ram pressure, $F_{p(i,j)}$) and the surface roughness controlled wind friction ($F_{f(i,j)}$)

$$F_{w(i,j)} = F_{p(i,j)} + F_{f(i,j)} \tag{2}$$

The common drag equation (Batchelor 1967) was used to calculate the two parts of Eq. 2. In order to determine the pressure force caused by the topography, Eq. 3 is used, containing the following variables: ρ the air density (1.23 kg/m^3), c_d the drag coefficient (set to 1), v the wind speed, and $A_{i,j}$ the effectively loaded area. The effectively loaded area is the projection of the topographic slope perpendicular to the wind direction, and was calculated for each cell separately. At any cell of the DTM having no upward slope in wind direction, the force was set to zero.

$$F_{p(i,j)} = \frac{\rho}{2} c_d v^2 A_{i,j} \tag{3}$$

$$F_{f(i,j)} = \frac{\rho}{2} c_{d(i,j)} v^2 A_0 \tag{4}$$

For the computation of the wind friction, the drag equation was used (Eq. 4). The loaded area A_0, being the effective surface of the DTM, was set to 625 m^2. The drag coefficient ($c_{d(i,j)}$) is a function of the surface roughness, which depends on the land use. This is given by the land use model (Fig. 4, "BASIS-DLM" BKG; Basis-DLM 2010), which has the same spatial resolution as the DTM, 25 m. The used drag coefficients (0.5 for forest, 0.05 for settlements, 0.005 for grassland and fields and 0.0 for water surfaces) are typical values used in meteorology.

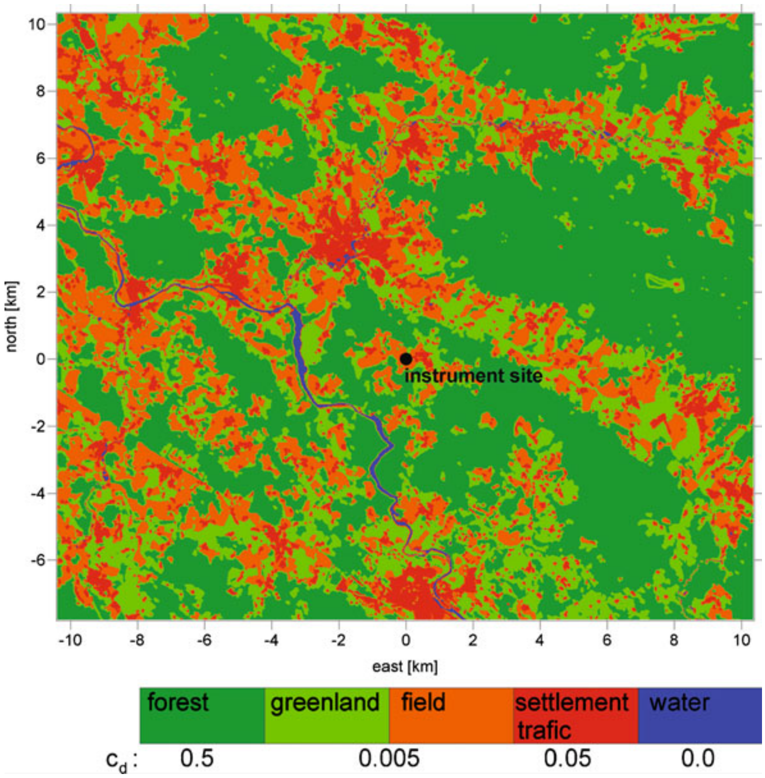

Fig. 4 Land use distribution of the modelled area. The drag coefficients of the different fields are given below

In order to determine the range of influence of the load, another set of computations was performed using a circular load mask of varying radius centred at the instrument site. Outside the mask the load was set to zero.

4 Computation scheme

Once the model is parameterized, the resulting deformation is a function of the wind speed and direction. In order to obtain a matrix which describes the effect of both variables, deformation fields were calculated for wind directions in 5° step from 0° (north wind) to 355° and wind speeds from 1 to 16 m/s in steps of 1 m/s. In a first run, only the pressure effect on the topography was considered. In a second run, both ram pressure and wind friction were taken into account. In this way a total number of 2,304 scenarios were computed.

For the conversion of the displacement fields into rotations, several steps are needed. At first, a selected set of about 10 nodes from the calculated displacement distributions in the area of interest was used to calculate the rotations in the three directions of space:

- Around the vertical (horizontal rotation)
- Tilt in east–west direction and
- Tilt in north–south direction.

The derivation of the rotations from the node displacements was done according to the method of Spudich et al. (1995) for each solution. This procedure yields matrices of rotation angles along the three axes depending on the wind direction and speed (Fig. 5).

In the next step, real wind data, recorded at the Wettzell meteo station with a sample rate of 1 min, were included to obtain a time series that can be compared to the ring laser and tilt observations. For each data point, the rotation caused by this specific wind speed and direction was taken from the rotation angle matrix (Fig. 5), resulting in a time series of wind-induced rotations having the unit radians. In order to compare it with the ring laser time series having the unit radians per second, there basically are two possible ways: integration of the observed Sagnac signal or differentiation of the calculated

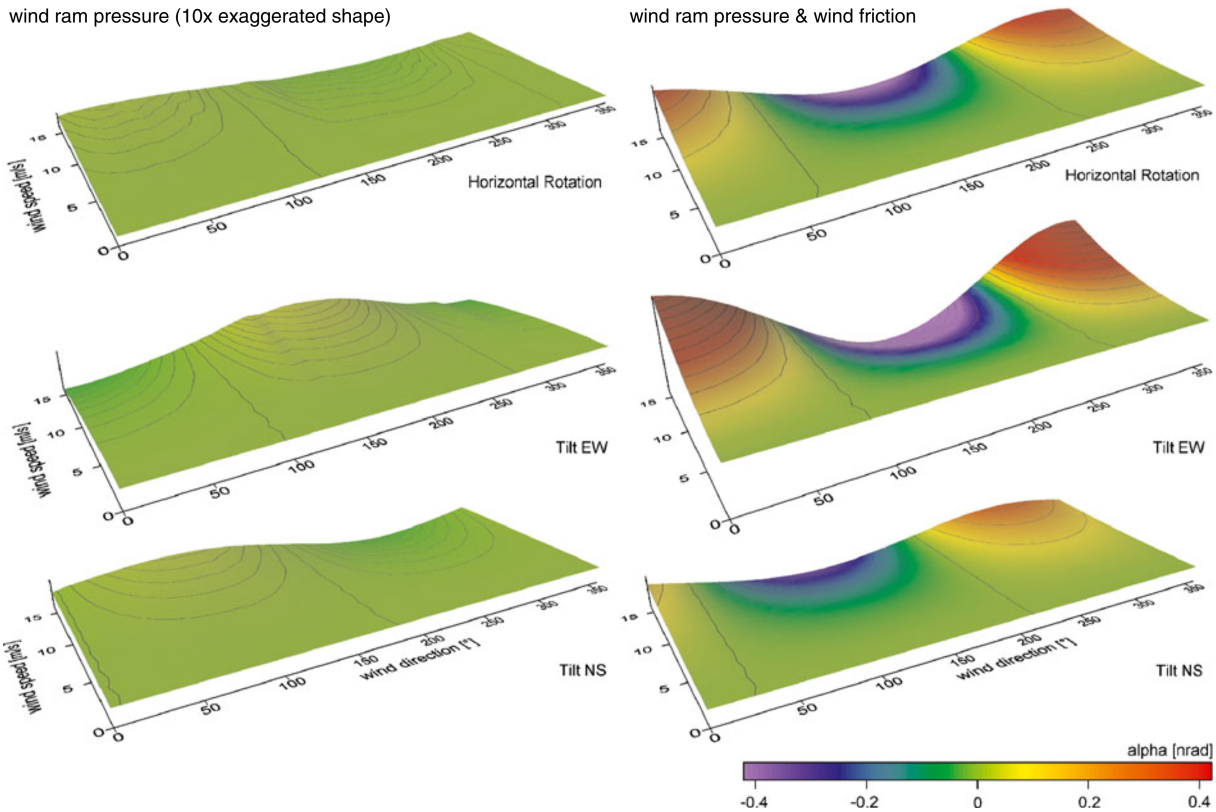

Fig. 5 Modelled rotation angles for wind ram pressure acting on the topography (*left*) and for wind ram pressure plus wind friction considered (*right*). The wind direction range from 0° (north wind) to 355° in 5° steps and wind speed varies between 0 and 16 m/s

wind-induced effect. Since the integration introduces additional noise, the differentiation of the synthetic wind effect time series was used, so that both time series show units of picorad per second.

The time series obtained in this way is compared to the observed Sagnac signal, which has been processed as follows. First, the signal was corrected for known and well-modelled signals, such as the effect of tidal tilt and polar motion. Secondly, the time series was resampled to the sample rate of the wind data, which is 1 min, using a high-pass filter. Tests have shown that the use of different cut-off frequencies (5 min up to 2 h) results in nearly the same signal. Hence it can be concluded that the wind-forced rotations act mainly in the short period range below 5 min. For further analysis, the observational data were de-noised using the waveshrink procedure as described in Shumway and Stoffer (2006) using the waveslim R package.

The waveshrink method is a powerful non-parametric smoother. Due to its adaptive nature, it is especially useful for time series which contain (noisy) blocks or bumps, like seismic time series, or the Sagnac series in this paper (Donoho and Johnstone 1995). The concept behind the waveshrink procedure is to reduce noise by shrinking the wavelet coefficients in the wavelet transform of the time series and then re-estimating the signal with the new coefficients. The threshold is chosen as $\lambda = \widehat{\sigma}\sqrt{2\log n}$, where n is the number of time steps in the series and $\widehat{\sigma}$ denotes the MAD, a robust estimate of the scale of the noise (the MAD is the median of the absolute deviations from the data's median.)

5 Results

The visualisation of the computed rotation angle matrix (Fig. 5) shows a continuous and smooth change of the values without discontinuities. This indicates that numerical artefacts caused by the mesh, the boundary conditions or the load are insignificant.

When comparing the computed rotation angles resulting from ram pressure alone (Fig. 5, left) and ram pressure plus wind friction (Fig. 5, right), the magnitude is clearly dominated by the wind friction effect, while the ram pressure effect is about one order of magnitude smaller. Additionally the dependency of the rotation angles on the wind direction is completely different for both load cases. This is not surprising, since two completely different model properties control the transfer of shear forces to the model, topography and drag coefficient/land use.

For each component, horizontal rotation, east–west and north–south tilt, there is a strong dependency on the wind direction. In the case of wind friction, the maximum effect occurs for winds coming from south and north. The zero crossings close to 90° and 270° show that there is only a weak effect coming from east–west winds. However the tilt in east–west direction shows the strongest effect and reaches a maximum in the order of 0.4 nrad for north–south-directed winds. In north–south direction, the tilt reaches only 0.2 nrad at a wind speed of 16 m/s, which is too little to affect the ring laser by its change in orientation. A minimum of about 10 nrad is required in order to affect the ring laser signal, the Sagnac frequency. The horizontal rotation angle reaches a maximum of 0.3 nrad, which can be detected by the ring laser if the signal builds up within a few seconds or tens of seconds.

The computations using a circular load mask of varying size show that the wind-forced deformations are very locally induced. The wind load applied to a disc of 200 m radius generates roughly 95% of the deformation when the entire model is loaded.

The comparison between the observed and the modelled rotation rates is shown in Fig. 6. The model is able to correctly reproduce the amplitudes and waveforms of the observation. The residual Sagnac signal has usually a noise level of 15 picorad/s peak to peak. The distribution of the residuals is non-normal, indicating that not all effects have been captured by the model. The distribution is leptokurtic (more acute than normal), with residual values strongly centred around zero and few strong but singular outliers. During windy periods, the noise swells up to the same order of magnitude as the calculated wind effect, up to 100 picorad/s. The sharp needles in the Sagnac signal that are not corresponding to a wind event in the rotation model are clearly identified as the rotation component of earthquake generated surface waves.

6 Discussion

For the east–west and north–south tilt components, it can be summarized that the wind-induced tilt effect plays a minor role. Having magnitudes usually far below 1 nrad, it is at or below the detection limit of high resolution tiltmeters. The impact of thunderstorms on tiltmeters must have different reasons like air mass attraction or barometric loading. During such events, barometric pressure and temperature can change rapidly, which affects the observation in a complex way. Barometric loading may cause tilts in the order of several nanoradians (e.g. Rabbel and Zschau 1985; Gebauer et al. 2010).

For the "G" ring laser however, the small wind-induced rotation angles of a tenth of a nanoradian around the vertical are clearly detectable, since the rotations happen fast and ring lasers are sensitive to the rotation rate rather than to the rotation angle. There is a good correlation between the modelled wind-induced rotations and the high-frequency component of the measured rotation rate when assuming realistic boundary conditions like elastic parameters and drag coefficients, and even the amplitude has a similar magnitude. However, subtracting the modelled wind-induced rotations from the measured time series does not produce a significant reduction of the wind noise due to a misfit of the phases. As wind is strongly variable in direction and amplitude on much smaller scales, this investigation suffers from temporal and spatial undersampling of the wind data.

Due to the elastic rheology, the amplitude of the modelled wind effect can be scaled linearly by the material parameters and by the load. The sensitive parameters for the load transfer are given in Eqs. 2 and 3—air density, drag coefficient and effectively loaded area. The air density scales the resulting force linearly for both load cases. It changes by 20% when the temperature varies from −25°C to 35°C. This can have a considerable effect on the amplitude of the calculated wind-induced rotations. The second sensitive parameter is the drag coefficient in the friction part (Eq. 3). It can vary by several orders of magnitude, depending on the land use. This may have a major impact on the result, especially when considering changes in land use or different coverage with vegetation during the seasons. For the wind pressure load, the drag coefficient is fixed to 1 in our model. However, the effectively loaded area depends on the

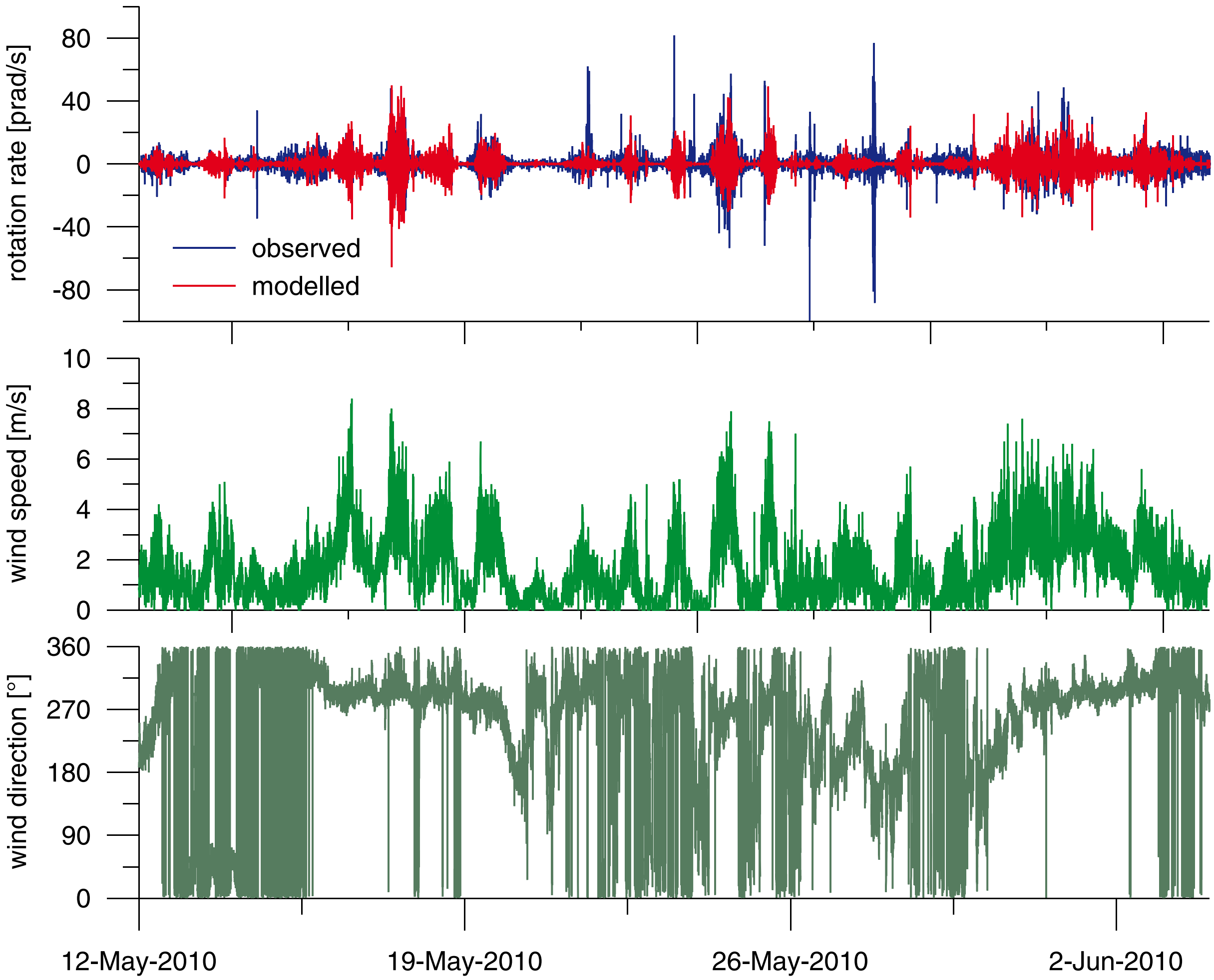

Fig. 6 Comparison between high-pass filtered rotation rate measurements with calculated rotation rates derived from the rotation matrices (Fig. 4), containing both ram pressure and wind friction effects. The directly observed wind parameters are shown below. The time period is from 12 May 2010 to 5 June 2010

used topographic model. A coarse model generally flattens the topography, while in a detailed model, more and more obstacles become effective and increase the loaded area.

It is shown that the deformation by wind is a very local effect. The modelled rotation angles of all three components change quickly when moving away from the observation site. The transferred shear force is strongly controlled by the distribution of forest and grassland, as the drag coefficients differ by a factor of 100. A frequent change of forest and grassland is typical for the Wettzell area, causing a very inhomogenous load distribution and thus a high dependency on the location.

7 Conclusions

The presented finite element model with a spatial resolution of 25 m yields realistic deformations induced by wind ram pressure and surface friction, explaining the high-frequency rotation component in the "G" ring laser. The consideration of a detailed topography and a surface friction term are the main reasons why about three orders of magnitude greater effects were computed as compared to the regional 1,000 × 1,000-km model of Velikoseltsev et al. (2009) with a horizontal resolution of 7 km. Another reason is the fact that long periodic wind effect, ranging from hours to days, was investigated in his work. The slower an angular change happens, the smaller is the resulting rotation rate.

A general problem when modelling the geological underground is the poor knowledge of the detailed situation with respect to material parameters, inhomogeneities or discontinuities like fractures or faults. These local site conditions may considerably affect the resulting deformations (e.g. Gebauer 2009). These conditions are largely unknown, thus assumptions and simplifications of the real conditions were made. However, the good correlation between the modelled wind-induced rotations and the measured rotation rate justifies the assumption that an inhomogenous rock body crossed by numerous discontinuities can be modelled by a homogenous body of reduced stiffness.

Another issue is the crude sampling rate of the local wind data of 1 min. The installation of a higher sampling wind sensor close to the ring laser facility will account for quickly changing wind conditions and provide a good base to remove the high-frequency wind effects from the ring laser data. If the static approach used in this model should not be appropriate to model the higher frequency wind effects, a dynamic approach could be required (Zürn et al. 2007).

It has been shown that wind-induced rotations affect the ring laser in the short periodic domain, thus being a disturbing signal in investigations in rotational seismology (Hadziioannou et al. 2011; Gebauer et al. 2010). A careful modelling of the wind effects at this specific site helps removing disturbing signal in the ring laser time series, making this instrument even more suitable for rotational seismology.

Acknowledgement This study is funded by the German Research Foundation (DFG) under the Project SCHR 645/2-3 which is gratefully acknowledged.

References

Abaqus Inc. (2007) ABAQUS documentation, version 6.7.

Altair Engineering, Inc. (2008) www.altair.com. Accessed 21 October 2008

Basis-DLM (2010) Digital LAND use Model 1:25000 Federal Agency of Cartography and Geodesy. http://www.geodatenzentrum.de. Accessed 1 May 2010

Batchelor GK (1967) An introduction to fluid dynamics. Cambridge University Press, New York

Donoho DL, Johnstone IM (1995) Adapting to unknown smoothness via wavelet shrinkage. J Am Stat Assoc 90 (432):1200–1224

DTM-25 (2010) Digital Terrain Model 1:25000. Federal Agency of Cartography and Geodesy. http://www.geodatenzentrum.de. Accessed 1 May 2010

Emeis S, Zilitinkevich SS (1991) Resistance law, effective roughness length, and deviation angle over hilly terrain. Bound Lay Meteor 55(1–2):191–198

Emeis S (1987) Pressure drag and effective roughness length with neutral stratification. Bound Lay Meteor 39(4):379–401

Gebauer A (2009) The impact of topographic and geological features on deformations of the upper crust. Dissertation, Friedrich-Schiller-University Jena. http://www.db-thueringen.de/servlets/DocumentServlet?id=14899. Accessed 10 July 2011

Gebauer A, Steffen H, Kroner C, Jahr T (2010) Finite element modelling of atmosphere loading effects on strain, tilt and displacement at multi-sensor stations. GJI 181(3):1593–1612. doi:10.1111/j.1365-246X.2010.04549.x

Hadziioannou C, Gaebler P, Schreiber U, Wassermann J, Igel H (2012) Examining ambient noise using co-located measurements of rotational and translational motion. J Seismol (this issue)

Igel H, Nader M-F, Kurrle D, Ferreira AM, Wassermann J, Schreiber KU (2011) Observations of Earth's toroidal free oscillations with a rotation sensor: the 2011 magnitude 9.0 Tohoku-Oki earthquake. Geophys Res Lett. doi:10.1029/2011GL049045

Klügel T (2001) Analyse der Zeitreihen lokaler Rotationssensoren - Entwicklung eines Orientierungsmodells - Schlussbericht DFG-Forschungsprojekt ROT-SKOP (SCHN 240/6), 78, Wettzell, http://www.fs.wettzell.de/publ/publ/ROT-SKOP_schlussbericht.pdf. Accessed 20 July 2011

Klügel T (2002) Tilt variations at shallow depth: implications for the installation of a laser gyroscope at the Geodetic Observatory Wettzell. Bull d'Inf Marées Terr 137:10927–10930

Klügel T, Schreiber U, Schlüter, Velikoseltsev A (2008) Advances in inertial Earth rotation measurements—new data from the Wettzell G ring laser. Proceedings of the "Journées Systèmes de Référence Spatio-temporels 2007", Observatoire de Paris, 17-19 September 2007, eds. Nicole Capitaine, ISBN: 978-2-901057-59-8, 173-176.

Kroner C, Jahr T, Kuhlmann S, Fischer KD (2005) Pressure-induced noise on horizontal seismometer and strainmeter records evaluated by finite element modelling. GJI 161:167–178

Kümpel HJ (1982) Tilt measurements. What do they tell us? Terra Cognita 2:391–399

Rabbel W, Zschau J (1985) Static deformations and gravity changes at the earth’s surface due to atmospheric loading. J Geophys 56:81–99

Schreiber U, Klügel T, Stedman GE (2003) Earth tide and tilt detection by a ring laser gyroscope. J Geophys Res 108 (B2):2132. doi:10.1029/2001JB000569

Schreiber KU, Velikoseltsev A, Rothacher M, Klügel T, Stedman GE, Wiltshire DL (2004) Direct measurement of diurnal polar motion by ring laser gyroscopes. JGR 109(B6):B06405

Schreiber U, Klügel T, Velikoseltsev A, Schlüter W, Stedman G, Wells JP (2009) The large ring laser G for continuous earth rotation monitoring. Pure Appl Geophys 166(8):1485–1498. doi:10.1007/s00024-004-0490-4

Schreiber U, Klügel T, Wells J-PR, Hurst RB, Gebauer A (2011) How to detect the chandler and the annual wobble of the earth with a large ring laser gyroscope. Phys Rev Lett 107 (17):173904. doi:10.1103/PhysRevLett.107.173904

Shumway RH, Stoffer DS (2006) Time series analysis and its applications. Springer. ISBN: 978-0387293172

Spudich P, Steck LK, Hellweg M, Fletcher JB, Baker LM (1995) Transient stresses at Parkfield, California, produced by the M 7.4 Landers earthquake of June 28, 1992: observations from the UPSAR dense seismograph array. J Geophys Res 100(B1):675–690

Stedman GE (1997) Ring laser tests of fundamental physics and geophysics. Rep Prog Phys 60:615–688

Steffen H (2006) The importance of instrument location on barometric pressure-induced noise. Bull d'Inf Marées Terr 141:11293–11302

Suryanto WJ, Wassermann J, Igel H, Cochard A, Vollmer D, Scherbaum F, Velikoseltsev A, Schreiber U (2006) First comparison of seismic array derived rotations with direct ring laser measurements of rotational ground motion. Bull Seism Soc Am 96(6):2059–2071. doi:10.1785/0120060004

Velikoseltsev A,Schreiber U, Klügel, Voigt TS, Graham RD (2008) Sagnac Interferometry for the Determination of Rotations in Geodesy and Seismology, 15th St. Petersburg International Conference on Integrated Navigation Systems, St. Petersburg

Velikoseltsev A, Schreiber U, Klügel T (2009) Modelling of episodic-transient signals in measurements of large ring lasers. Final report of the DFG research project SCHR 645/2 (MOD-TRANS). Technical University Munich

Weise A (1992) Neigungsmessungen in der Geodynamik - Ergebnisse von der 3-Komponenten-Station Metsähovi. Technical University Clausthal, Dissertation

Zürn W, Exß J, Steffen H, Kroner C, Jahr T, Westerhaus M (2007) On reduction of long-period horizontal seismic noise using local barometric pressure. GJI 171(2):780–796. doi:10.1111/j.1365-246X.2007.03553.x